Upscaling the permeability properties using multiscale X-ray-CT images with digital rock modeling and deep learning techniques

Fei Jiang[1,2,3], Yaotian Guo[1], Takeshi Tsuji[3,4],Yoshitake Kato[5], Mai Shimokawara[5], Lionel Esteban[6], Mojtaba Seyyedi[6], Marina Pervukhina[6], Maxim Lebedev[7], Ryuta Kitamura[5]

[1]Department of Mechanical Engineering, Yamaguchi University, Ube, Japan
[2]Blue energy center for SGE technology (BEST), Yamaguchi University, Ube, Japan
[3]International Institute for Carbon-Neutral Energy Research (WPI-I2CNER), Kyushu University, Fukuoka, Japan
[4]Department of Systems Innovation, Faculty of Engineering, the University of Tokyo, Tokyo, Japan
[5]JOGMEC, Chiba, Japan
[6]CSIRO Energy BU, Perth, Australia
[7]Curtin University, Perth, Australia

Key Points:

- A workflow is proposed to estimate the upscaled absolute permeability of the rock core direct from CT images.
- A deep learning technique is adopted to establish correlations between high-resolution computed permeability and low-resolution images.
- The upscaling method allows estimating the large-scale permeability while preserving the effects of fine-scale permeability variations.

Corresponding author: Fei Jiang, fjiang@yamaguchi-u.ac.jp

Abstract

This study presents a workflow to predict the upscaled absolute permeability of the rock core direct from CT images whose resolution are not sufficient to allow direct pore-scale permeability computation. This workflow exploits the deep learning technique with the data of raw CT images of rocks and their corresponding permeability value obtained by performing flow simulation on high resolution CT images. The permeability map of a much larger region in the rock core is predicted by the trained neural network. Finally, the upscaled permeability of the entire rock core is calculated by the Darcy flow solver, and the results showed a good agreement with the experiment data. This proposed deep-learning based upscaling method allows estimating the permeability of large-scale core samples while preserving the effects of fine-scale pore structure variations due to the local heterogeneity.

1 Introduction

The flow behavior in porous rocks plays a vital role in many scientific and engineering fields, such as oil and gas recovery (Lake et al., 2014), geothermal energy (Tester et al., 2006), and geologic carbon storage (Juanes et al., 2006). The permeability property is the most important parameter to characterize the fluid transport in porous media, which strongly depends on the pore structure. The heterogeneity of pore structure usually varies significantly across a wide range of length scales, which leads to scale dependence of permeability (Worthington, 2004). The issue of scale and heterogeneity make the prediction of permeability extremely difficult.

With the availability of three-dimensional imaging techniques, we are able to investigate the detailed structural heterogeneity of rocks at different scales: at the nano (nm) scale using nano-CT imaging (Goral et al., 2019), at the pore (μm) scale using micro-CT imaging (Blunt et al., 2013), and at the core (cm) scale using medical-CT imaging (Zhai et al., 2020). However, very few studies have been conducted on establishing linkage among these scales (Dehghan Khalili et al., 2013; Menke et al., 2021), and the scaling behavior of permeability is difficult to predict. Khalili et al. (2013) focus on carbonate reservoir rock and investigate the use of porosity-permeability relationships derived from micro-CT images to estimate permeability on a larger scale by the renormalization technique. More recently, Menke et al.(2021) applied the multivariate regression method to upscale and predict permeability from the pore scale to the Darcy-scale by deriving an upscaled porosity-permeability relationship. However, no studies have yet estimated the upscaled permeability directly from the large-scale raw CT images with low resolution. The lower resolution CT images provide greater sample coverage, therefore it is able to capture more sample heterogeneity, but do not adequately represent the correct pore structure, which is essential for computing the permeability using the direct simulation method (Botha & Sheppard, 2016). Previous studies (Fredrich et al., 1993; Pape et al., 1999) have proven that absolute and relative permeability are strongly dependent on pore space geometry. Therefore, accurate flow and other physical properties can only be obtained by carrying out physical simulations on high-resolution CT images that accurately represent the pore geometries and characterize all major flow paths in the rock. Arns et al. (2001) investigated the effects of image resolution on the computation of electrical conductivity. They observed that low image resolution causes the over-estimation of the formation factor. On the other hand, the high-resolution CT images are able to resolve well the pore structure permitting direct simulation of fluid flow and accurately estimate the permeability property (Jiang & Tsuji, 2017; Blunt et al., 2013; Shah et al., 2016). Direct simulations like Lattice Boltzmann Methods (LBM) or Finite Volume Methods (FVM) to solve the Navier Stokes Equation (NSE) can be performed at the pore spaces of rocks extracted from the high-resolution CT images (Raeini et al., 2012; Jiang & Tsuji, 2014, 2015, 2017). However, the direct simulation requires a large amount of computational resources and is time consuming. In addition, high resolution leads to a smaller

field of view and can only cover a small representative volume for the very homogeneous rocks. For rock samples exhibiting heterogeneity above the field of view, a low-resolution CT image with large sample coverage is required. However, the low-resolution images cannot provide enough accuracy for the computation of physical properties. Therefore, integration of the physical informations obtained from high-resolution CT images at a small scale into the low-resolution CT image data at a large scale is an efficient way to improve the prediction accuracy of the permeability. To systematically propagate the effects of small-scale geological variations observed in high-resolution CT images up to the large core-scale low-resolution CT images, we need an upscaling method. The upscaling requires developing a reliable equivalent model on a coarser scale, which can represent the behavior of fine-scale model in an averaged sense. The homogenization theory is a widely used upscaling technique that can compute an effective property for periodic structures (Z.-J. Xu, 2012). However, it is doubtful whether such a mathematical homogenization process can be used to model the permeability of natural rocks because they are rarely periodic. A reliable upscaling process requires analyzing the wealth of imaging data in order to characterize the inherent rock heterogeneities at multiple scales (Menke et al., 2021).

Recently, the deep learning technology holds a solid potential to extract the characteristics of pore geometry from the CT images (Bizhani et al., 2022). The features of rock CT images have been investigated using various neural networks (Da Wang et al., 2019) with many extended applications (Wang, Blunt, et al., 2021). For instance, the synthetic rock image reconstruction has been successfully performed by using the Generative Adversarial Networks (GAN), which reproduces the similar characteristics of natural rocks (You et al., 2021). In addition, the 3D image-based digital rock physical modelling can also be enhanced with deep learning techniques to predict petrophysical properties such as permeability (Suzuki et al., 2022), relative permeability and the distribution of fluid phases (Wang, Blunt, et al., 2021). Santos et al. (2020) used a convolutional neural network (CNN) to predict the flow velocity fields inside the pore spaces directly. Rabbani and Babaei (Rabbani & Babaei, 2019) successfully estimated the permeability of the pore-network model from the geometric properties using a regression method based on an Artificial Neural Network (ANN). Alqahtani et al.(2021) predicted the permeability directly from the CT images by 3D CNN regression. However, very few studies have been conducted on applying of deep learning techniques to upscale permeability. This study aims to combine the deep learning technique and digital rock physics to predict the permeability of large-scale core with the information from the small-scale micro samples. The 3D CNN based deep learning techniques are used to establish correlations between low-resolution image characteristics and high-resolution computed permeability by overlapping registered CT images derived at different resolutions spanning orders of magnitude in length scales. The CNN networks are trained using the dataset of directly calculated permeability values based on high-resolution CT images and the corresponding low-resolution raw images. Then, a workflow is proposed to predict and map the absolute permeability variations over the large fields of view from the low-resolution images by the trained CNN networks. Finally, the upscaled permeability is calculated by inputting the predicted permeability map at the whole core scale into a Darcy flow solver. Our proposed upscaling approach benefits from both the large field of view by the low-resolution CT and the high accuracy of flow property computation by the high-resolution CT.

2 Rock samples

A Boise sandstone core was used in this study as it offers a range of pore size, grain size, mineralogy, and geological structures that are not too complex for modelling purposes of permeability upscaling. Boise is sandstone with 40% quartz and about 50% feldspars with a brine porosity and permeability at about 24% and 2.8D, respectively. The pore

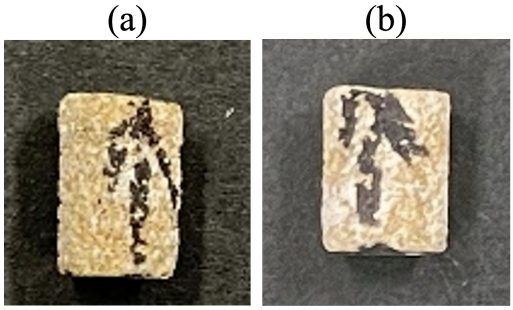

Figure 1. Boise sandstone: (a) sample I (b) sample II.

size distribution is around 50 μm, and the grain size distribution is around 100 μm, which are measured from thin section optical images. Here, we extracted two small core samples (samples I and II) with a diameter of 6.8mm out of the whole meter scale rock sample (Fig. 1). These two small samples have lengths of about 1.0 cm. Micro X-ray CT imaging for these samples was conducted using the micro CT scanner (Xradia Versa XRM-500) with two resolutions: $2\mu m$/voxel (fine) and $8\mu m$/voxel (coarse).

3 Method

The permeability upscaling method mainly contains three parts: (1) build a neural network trained by the datasets consisting of pairs of the sub-volumes from the coarse scanned 3D CT images (low resolution) and their corresponding permeability value obtained by the direct flow simulation on fine scanned CT images (high resolution) (2) predict the permeability distributions directly from the coarse scanned 3D CT images of the whole core using the neural network; (3) calculate the upscaled permeability by Darcy-scale flow simulations using the predicted permeability map.

For the first part, we propose a workflow aimed at predicting absolute permeability direct from low-resolution images using a deep learning technique combined with direct flow simulation on high-resolution images. Calculating permeability directly based on the low-resolution CT is difficult because the low resolution usually causes connecting narrow pore throats to be represented by blurred grayscale values and leads to the limitation of obtaining the accurate pore structure in pore scale. Due to the inability of resolving high-quality pore structures, low resolution CT images are inadequate for direct flow simulation. Therefore, the accurate permeability data must be evaluated based on the high-resolution CT images. However, high-resolution usually leads to a small fields of view, which is inadequate for heterogeneous porous media. On the other hand, low-resolution micro CT images give larger sample coverage and are therefore more representative of heterogeneous systems on a large scale. Our proposed workflow involves computing permeability from high-resolution micro-CT images and registration of the corresponding low-resolution images on a large scale. This approach benefits from the accurate permeability data obtained from well-resolved pore structure at a small scale and large field of view characterizing the spatial heterogeneity. Deep learning regression techniques are used for predicting and mapping permeability variations in larger-scale low-resolution images. Binarization of the low-resolution images is unnecessary since the raw images data can be directly input into the deep learning neural network using CNN. Once the neural network is trained with the dataset of directly calculated permeability values and corresponding low-resolution raw images, we are able to predict the permeability map over the whole domain of the large sample. Finally, the upscaled permeability

of the entire rock core can be calculated by the Darcy flow solver based on the permeability map. The detailed workflow contains the following steps (Fig. 2):

1. Micro-CT coarse scanning of the whole core (1.0 cm in length) with low resolution ($8\mu m$/voxel) (left-hand side image in Fig. 2 (a));
2. Selection of location for close-up view region (2 mm wide) and micro-CT fine scanning with high resolution at the pore-scale ($2\mu m$/voxel) (right-hand side background image in Fig. 2 (a));
3. Noise reducing and segmentation of the fine scanned micro-CT images (black-white area of the right-hand side image in Fig. 2 (a));
4. Extracting of sub-volumes (grids in Fig. 2 (a) right) from the segmented images with high resolution ;
5. Calculation of permeability properties from the extracted high-resolution sub-volumes using LBM;
6. Identifying the same area of sub-volumes on the coarse scanned images of the whole core (registration of the overlap region at different resolutions) (Fig. 2 (a));
7. Linking the permeability data to the corresponding low-resolution area in coarse scanned 3D CT images and create the training datasets consisting of pairs of low-resolution 3D images and their corresponding permeability value;
8. Training the neural network with the prepared datasets (Fig. 2 (b));
9. Predicting the permeability map of the whole core by the trained neural network (Fig. 2 (c));
10. Calculating the flow flux inside the whole core by Darcy flow solver (Fig. 2 (d)); and
11. Estimate the upscaled permeability of the whole rock core area.

In this method, the CNN regression model establishes a relationship between low-resolution images and high-resolution computed permeability. In such a way, the highly accurate information obtained from small-scale high-resolution images can be upscaled to a large domain. This approach has great potential to enable the upscaling of any physical properties from small pore scales to large core scales.

3.1 Training dataset acquisition

The whole sample was first imaged by the micro-CT scanner with low resolution ($8\ \mu m$) to cover the entire core area (Fig .3). Then the center area of the sample was selected as ROI (region of interest) and scanned with fine resolution ($2\ \mu m$). The fine resolution was determined to capture the pore structure well enough for calculating the permeability of the extracted sub-volumes using pore-scale flow simulation. To improve the image quality, a non-local means filter was applied to the fine CT images. The filter cancels most of the salt-n-pepper noise, making the image smoother and more uniform while preserving boundaries. Afterwards, the datasets of high-resolution underwent a segmentation routine for extracting the binary pore geometry. The segmentation is based on a simple threshold (histogram-based) algorithm which assigns labels to voxels according to their intensities. The threshold values were chosen based on the local minimum values of the histograms of the image intensities. Note that only high-resolution images need to be processed and segmented for direct flow simulation. In contrast, the original raw images with low resolution can be directly used for deep learning. Finally, a binarized pore-geometry model with voxels of $690\times690\times5000$ was cropped from the cylindric sample area and reconstructed (Fig .3). Then the binarized model was divided into small 200^3 sub-volumes (dark red cubes in Fig .3). This size of sub-volume is smaller than the size of the representative volume element (RVE), which is recommended for deep learning in order to increase the variety of sub-volumes in terms of porosity and permeability (Hong & Liu, 2020). To meet the the demand of large datasets, the sub-volumes are allowed to be overlapped with 100 voxels during the extraction (red grids in Fig .3). The

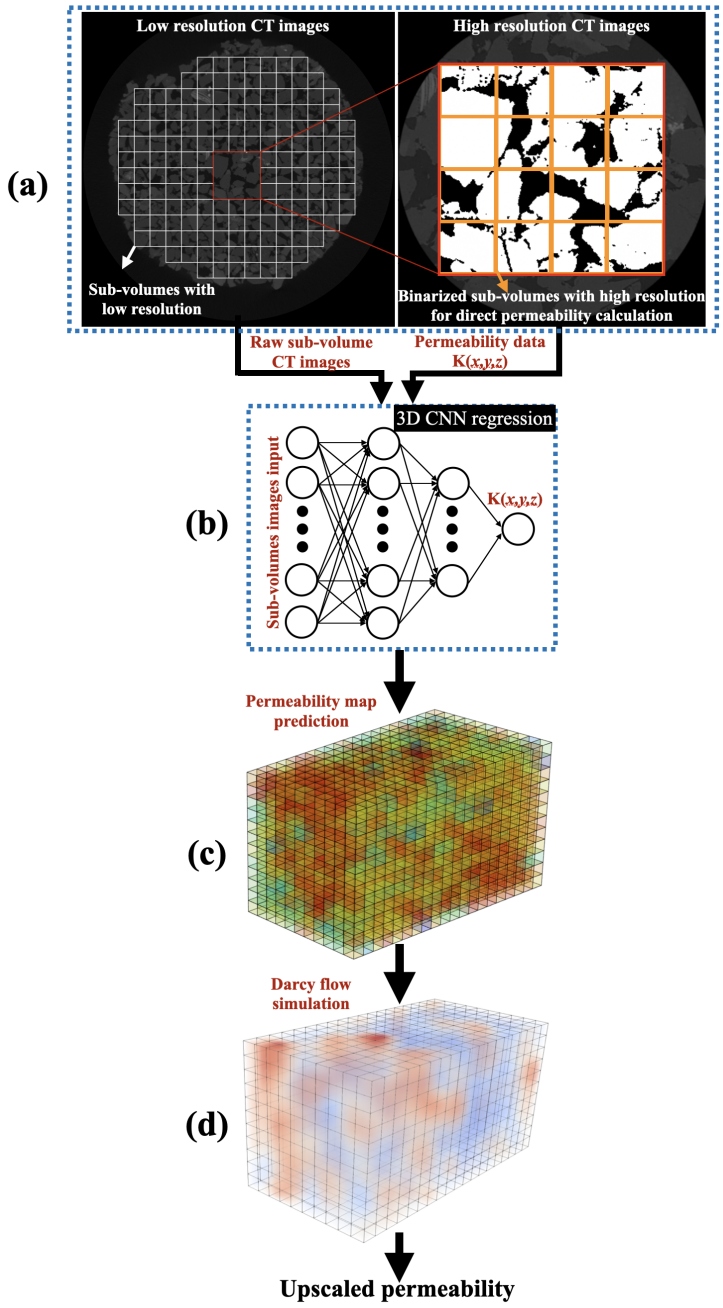

Figure 2. Permeability upscaling workflow: (a) micro-CT scanning and preparation of the training dataset; (b)neural network training with the prepared CT images and permeability data (c) predicted permeability map of the whole core by the trained neural network; (d)flow flux distribution inside the whole core calculated by the Darcy flow solver.

permeability of these sub-volumes was calculated by the LBM flow solver described in Section 3.3. The corresponding sub-volumes with low-resolution at the same location in the sample were then extracted directly from the original coarse-scanned images (grayscale cubes in Fig .3). Since the fine-scanned and coarse-scanned images have four times ($4\times$) resolution difference, the dimension of the low-resolution sub-volume is $50 \times 50 \times 50$. In this way, we obtained the dataset for deep learning consisting of pairs of a low-resolution sub-volume and its permeability value (black box in Fig .3). The total number of the sub-volumes is 8000 for each sample. In our study, 90% of the data are used as the training data while the rest 10% data are used for testing data.

3.2 Registration of images at different scales

For a single rock core sample, since the coarse scan with low resolution is conducted along with the fine scan with high resolution at different scales, we have to identify the same area at both resolutions. Therefore, the position of the sample was carefully set to keep the same scanning angle during the two scans for the convenience of image registration. Correlating the fine scanned data to coarse scanned data can be easily conducted with the reference CT slice of the same depth from the top of the core sample. An example of image registration across two length scales is shown in Fig.4, where the matching area with high resolution is shown for the same region in the low-resolution whole core images. In such a way, direct observation of the same property for the same domain at different resolutions becomes possible. The accurate registration of the center core into the whole core allows the information learned at a higher resolution but on a smaller volume to be upscaled into the whole. The corresponding sub-volume at low resolution is carefully searched in the whole core images to match the binarized high-resolution sub-volume.

3.3 Direct simulation for the acquisition of ground truth flow data

Recently, direct pore-scale simulation has been widely used to obtain flow properties from digital rock CT images (Boek & Venturoli, 2010; J. Yang & Boek, 2013; Jiang & Tsuji, 2017; L. Yang et al., 2019). In this study, we adopt the LBM to calculate the flow field in the complex pore spaces. The LBM is an efficient and accurate method for both single-phase and multiphase flow simulation (Liu et al., 2021; Li et al., 2021; Jiang et al., 2021; Zhang et al., 2022; Jiang et al., 2022) directly on the raw images of rocks. The LBM can approximately recover Navier Strokes equations from kinetic theory (Shan et al., 2006). In LBM, particle distribution functions (PDF) $f_i(\mathbf{x}, t)$ are introduced to represent the probability of encountering a fluid pseudo-particle with velocity $\mathbf{e}_i$ and spatial position $\mathbf{x}$ at time t.

$$f_i\left(\mathbf{x} + \mathbf{e}_i \delta t, t + \delta t\right) = f_i(\mathbf{x}, t) + \Omega_i(\mathbf{x}, t) \tag{1}$$

where $\mathbf{e}_i$ is the lattice velocity in the ith direction, δt is the time step, and Ω_i is the collision operator. A three-dimensional lattice with 19 velocity vectors (D3Q19) is used in the present study (Guo & Shu, 2013). To improve the numerical stability and remove the uncertainty due to viscosity-dependence (Pan et al., 2006), the multiple-relaxation-time (MRT) collision operator (d'Humières, 1992) is adopted.

Single-phase flow is simulated until the steady-state conditions are achieved. The steady state is determined by tracking the change of average velocity in pore spaces. When the relative change in average velocity is less than 10^{-5}, the simulation is considered to converge. The permeability can be calculated by

$$K = \frac{\mu \overline{v} L}{\Delta P} \tag{2}$$

where, $\overline{v}$ is the mean velocity in the flow direction, μ is the kinematic viscosity of the fluid, L is the length of the domain along the flow direction, and ΔP is the pressure difference

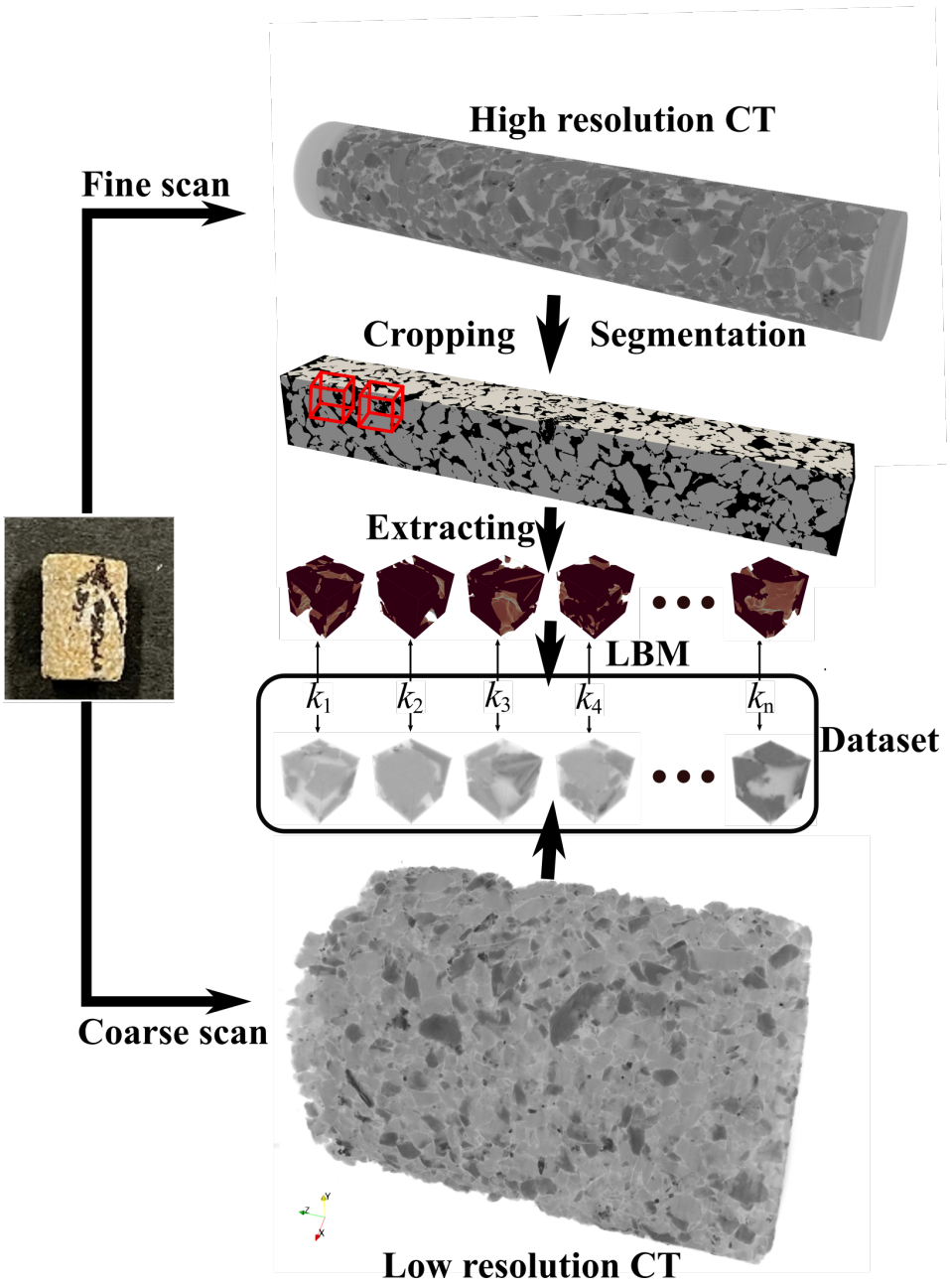

Figure 3. Workflow of training dataset acquisition. The dataset consists pairs of low resolution sub-volumes and its permeability value calculated by LBM solver based on the corresponding high resolution sub-volumes.

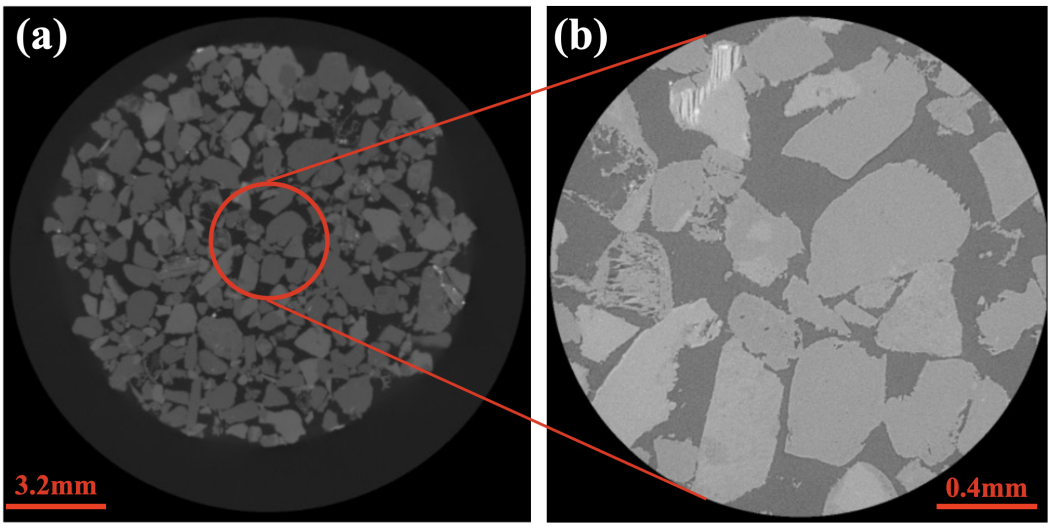

Figure 4. Registration of micro-CT images with two different resolutions: (a) low resolution CT for whole rock core (b) high resolution CT for center core region.

between the inlet and outlet. In our simulation, a constant pressure drop between inlet and outlet is applied by using a body force mimicking the local pressure gradient, and the no-slip wall boundary conditions are imposed on the grain surfaces. The pressure gradient is set sufficiently low to ensure the Reynolds number small enough to reproduce Stokes-regime flow. We applied a periodic condition at all outer boundaries of the core cube. Specifically, for the flow direction, the sample was mirrored to ensure that the pore spaces on the right side were connected to the left side.

3.4 Convolutional neural networks for predicting permeability

The convolutional neural network (ConvNets) (LeCun et al., 1998) is the basis of typical deep learning models, which consist of a sequence of nonlinear transformations implemented as convolutional layers (N. J. Alqahtani et al., 2021). In this study, six network architectures of ConvNets: Conv8, VGG16, VGG19 (Simonyan & Zisserman, 2014), GoogLeNet-V1, GoogLeNet-V3 (Szegedy et al., 2015), ResNet34 (He et al., 2016) are adopted for permeability prediction. The details of those network architectures are presented in Appendix A. The most simple Conv8 network consists of four convolution blocks, including a 3D convolutional layer, batch normalization(Ioffe & Szegedy, 2015), and a rectified linear unit (ReLU)as a activation function (Nair & Hinton, 2010), followed by a Global Average Pooling layer (GAP) and four dense layers (Fig. A1). The final convolutional layer was vectorized by the GAP layer and then fed into fully connected dense layers. The function of the GAP layer is to bridge the convolutional structure with traditional neural networks. The 3D CNN enables obtaining the feature map containing volumetric contextual information in all three dimensions. In this study, the Conv8 is the most shallow network for performance comparison.

VGG (Simonyan & Zisserman, 2014) is a deeper version of the ConvNet architecture (Fig. A2 and A3). In VGG, only the 3×3×3 size of the convolution layer filter is used. Such a small-scale convolution filter helps accelerate the learning process. The activation function with ReLU is always added after the convolution layer. VGG16 is a network of 16 layers deep and consists of five max-pooling layers in each convolution block. Three dense layers are applied before the output layer. The architecture of VGG19 is

similar to the VGG16, except the network is 19 layers deep (3 more convolutional layers).

GoogLeNet (Szegedy et al., 2015) introduced the concept of the inception module (network-in-network), which is built by a combination of small-scale convolution layers (Fig. A4 and A5). In this inception module, multiple convolution layers with different sizes (1×1, 3×3, 5×5) are applied in parallel and the outputs of each convolution layer are then concatenated. Usually, to realize a deeper and more expressive network, the number of weights significantly increases, resulting in a longer training time. By the introduction of a module consisting of a bunch of small convolution filters, GoogLeNet achieves a good trade-off between model performance and the number of weights, and the amount of computation cost can be greatly reduced. The improved V3 version of GoogLeNet decomposes 3×3 convolutions into two one-dimensional convolutions (1×3 , 3×1), which can both improve the calculation speed and increase the depth and nonlinearity of the network. In the original GoogLeNet, the auxiliary loss units are added to branch off from the middle of the network. The auxiliary loss unit can prevent gradient vanishing for classification problems by propagating the error directly to the middle layer of the network. In our regression problem, we modified the network by replacing the last 3 layers with a fully connected dense layer and a regression layer and removing the auxiliary loss unit.

The deeper layers caused the gradient loss problem and the degradation problem, making learning more difficult. ResNet (He et al., 2016) solves the gradient vanishing problem by introducing a mechanism called shortcut connection, which directly adds the inputs of the front layer to the back layer. The basic ResNet block contains two convolutional layers each, followed by batch normalization and a ReLU. The shortcut connection links the top of the basic block to just before the ReLU after the second convolutional layer in the block. This shortcut connection is able to skip the nonsucceeding layers for the very deep model.

In this study, all the networks are implemented using the TensorFlow machine learning platform (Abadi et al., 2015). The detailed structures of those used networks are explained in Appendix A.

3.5 Loss functions and accuracy measurements

During training, we used five loss functions to optimize the network model: Mean Squared Error (MSE), Mean Absolute Error (MAE), Huber loss, Mean Squared Logarithmic Error (MSLE) and Logcosh loss. The mathematical formula for computing each metric is shown in Table.1, where y_i represents the actual value of the ith sample, superscript p means the predicted value, and n for the number of samples in each dataset. MAE and MSE are the most common criteria for regression problems (Botchkarev, 2018). The Huber loss function has a quadratic form for small values of errors, and a linear form for large values of errors. The Huber loss can be considered as a combination of MAE and MSE, which returns to MAE when the loss is large and MSE when the loss is small. The δ in the Huber function means a measure of the spread of the inliers, which is set as 1.0 in our study. The disadvantage of the MSE is that it is sensitive to outliers because the larger the error, the more it overestimates the error. In contrast, MSLE, which uses logarithmic error, does not overestimate even when the error is large because of its logarithmic nature. The Logcosh loss is basically similar to MAE but gets closer to MSE when losses are small. Though we used different loss functions for training, only the MAE metric is used to assess the model accuracy because it is a common criterion for regression problems (Botchkarev, 2018).

Loss	Formula
MSE	$\frac{1}{n}\sum_{i=1}^{n}(y_i - y_i^p)^2$
MAE	$\frac{1}{n}\sum_{i=1}^{n}\ \lvert y_i - y_i^p\rvert$
Huber	$\frac{1}{n}\sum_{i=1}^{n}\ \frac{1}{2}(y_i - y_i^p)^2,\ if\ \lvert y_i - y_i^p\rvert \leq\ \delta$ $\frac{1}{n}\sum_{i=1}^{n}\delta \times (\lvert y_i - y_i^p\rvert - \frac{1}{2}\delta),\ if\ \lvert y_i - y_i^p\rvert >\ \delta$
MSLE	$\frac{1}{n}\sum_{i=1}^{n}\left(\log(y_i+1) - \log(y_i^p+1)\right)^2$
Logcosh	$\frac{1}{n}\sum_{i=1}^{n}\log\left(\frac{\exp\left(y_i^p - y_i\right) - \exp(y_i - y_i^p)}{2}\right)$

Table 1. Loss functions for the training process

3.6 Upscaling using Darcy flow solver for large scale sample

Since only the permeabilities of sub-volumes from the center core area were calculated by flow simulation, the remaining domain outside the center area was further divided into the same-size sub-volumes whose permeability can be predicted by the trained neural network. After the permeability map of the whole core is obtained, we can use the conventional Darcy flow solver to estimate the overall permeability of the whole core. In this study, we adopted the MATLAB Reservoir Simulation Toolbox (MRST) (Lie, 2019) to calculate the single-phase flow in the large core sample. The following governing equation for single-phase flow is solved by the two-point finite volume method in MRST:

$$\nabla \cdot \vec{v} = q, \quad \vec{v} = -\mathbf{K}\nabla P, \tag{3}$$

where, $\vec{v}$ is the Darcy velocity, q is the flux and $\mathbf{K}$ is the permeability tensor considering anisotropy. The sets of non-overlapped sub-volumes are directly used as the Cartesian grids in the Darcy flow solver. Fixed pressure boundary conditions are imposed on the inlet and outlet sides to generate a pressure gradient for driving the fluid. The no-flow conditions are applied on the rest of the boundaries. After the solver converged, the pressures for each grid and the flow flux across each face of the grid can be obtained. Finally, the upscaled permeability can be calculated from the flux of a single cross-section of the core sample.

4 Results and discussion

4.1 Permeability results of the direct flow simulation

The calculated permeability by the direct flow simulation is used as the training data for deep learning. Therefore, we first give detailed information about the permeability data for training. The histograms of the calculated permeability data for the sub-volumes (Fig. 5) indicate that the sample II has a much lower permeability compared with sample I. Most of the permeability values of sub-volumes in sample II are below 1.0 Darcy. The mean permeabilities are 10.8 Darcy and 5.03 Darcy for sample I and II, respectively. The standard deviation of permeability data for sample II is smaller than that for sample I, which means that the permeabilities are more concentrated in the low-value region for sample II. On the contrary, the permeabilities are widely distributed in sample I.

4.2 Evaluation of loss function

To examine which loss function gives the best performance in predicting permeability, we tested the five loss functions described in Section 3.5 using the basic Conv8 network. The accuracy for different loss functions is evaluated based on the MAE metric from test data of sample I.

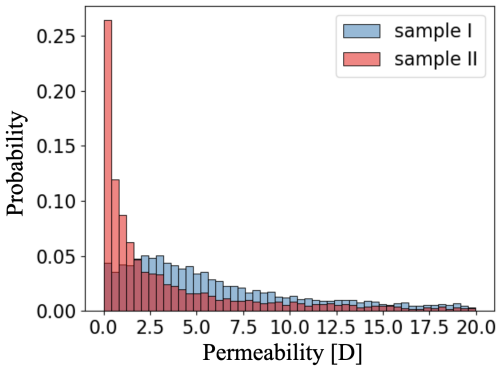

Figure 5. Histograms of the permeability for sample I and II.

Loss function	MSE	MAE	Huber	MSLE	Logcosh
Accuracy (MAE)	1.8957	1.9384	1.7639	2.8808	1.9488

Table 2. Accuracy of the five tested loss functions

The results (Table.2) show that the Huber loss function gives the best performance, which is in agreement with the reference (N. Alqahtani et al., 2020). The Huber loss is usually used for regression problems that are less sensitive to outliers (Huber, 1992). In our training data, some of the sub-volumes with high porosities have extremely large permeabilities which may have a significant effect on the training accuracy. The Huber loss function is able to suppress the effect of those high permeability data points. Therefore, we decided to adopt the Huber loss function for the training process in all other networks hereinafter.

4.3 Performance of different networks

The datasets of sample I are used for training the six neural networks described in Section 3.4 to find out which network gives the best performance. The predicted values of permeabilities are plotted against the actual permeabilities obtained by direct numerical simulation by different networks in Fig. 6 and 7 for Sample I. It can be seen that the GoogLeNet and Resnet have better performance compared with the conventional Conv8 and VGG networks for the training data set. For the test data set, the Resnet gives the best performance. Therefore, for sample II, only the results of Resnet are presented (Fig.8). The accuracy in terms of the MAE for each network using the testing data set are shown in Table.3 for both samples. With increasing the depth of the network, the accuracy is improved. However, there are only limited gains in accuracy when just increasing the layers of conventional networks (from VGG16 to VGG19). The reason is that the training process is performed by backpropagation method (Rumelhart et al., 1986), and it becomes more difficult to correctly propagate the error when using more layers. Besides, it is more easy to get stuck on a local optimum or saddle point during the training process if we simply add more CNN layers. Increasing the number of layers may also lead to overfitting. Resnet has a shortcut connection in the networks, which significantly improves the performance when using a deep network. Our results also show that the Resnet has the best performance with an MAE of 0.4546 and 0.2249 for samples I and II, respectively. It should be noted that the sub-volume with high permeability has a large contribution to the value of MAE. Because the sub-volumes with extremely high permeability are rare in the core, the learning accuracy is lower for these sub-volumes due

to the small number of their data sets (right-hand side figures in Fig. 7). The prediction error from those sub-volumes may lead to a relatively high MAE value. Compared to sample I, the permeabilities of sub-volumes in sample II are lower and more concentrated (Fig. 5), therefore the predicting accuracy for sample II is higher (Fig .8), and the MAE for sample II is lower than that for sample I (Table 3).

Model	Layer number	MAE (sample I)	MAE (sample II)
Conv8	8	1.4226	0.8016
VGG16	16	1.2031	0.6939
VGG19	19	1.1348	0.9163
GoogLeNet-V1	22	1.1729	0.6141
GoogLeNet-V3	25	0.7589	0.4332
Resnet34	34	0.4546	0.2249

Table 3. The accuracy (MAE) of regression for various neural networks with different depths and structures

4.4 Porosity prediction

In addition to the permeability, we also use the same approach to predict the porosities of the sub-volumes directly from the coarse scanned CT images. Here, we only use the Resnet34 for the porosity prediction because it has the best performance for predicting permeability. The corresponding training data for porosity was obtained from the same segmented sub-volume models used in the LBM direct flow simulation.

The predicted results (Fig.9 and 10) show that the porosity can be accurately estimated by the Resnet34 network. The MAEs of the test data with the trained networks are 0.00193 and 0.00152 for samples I and II, respectively. The predictive accuracy for porosity is much better compared with that for permeability. The reason is that the porosity only depends on the gray scale histogram, while the permeability also depends on the connectivity of pore spaces (e.g., the tortuosity of flow paths). Therefore, the porosity is much easier to be characterized by using deep learning, which also implies that the segmentation process can be tackled by the neural network (Wang, Shabaninejad, et al., 2021). With the trained network for porosity, we are also able to obtain the porosity map direct from the raw coarse CT images.

4.5 Permeability map predicted by the trained network

Since the Resnet has the best performance in terms of permeability prediction, we then estimated the permeabilities of the sub-volumes at the periphery of the rock core (white boxes in the left image of Fig.2) by inputting the raw low-resolution images into the trained Resnet network. The permeabilities of these unseen sub-volumes are predicted using the best models' weights of Resnet. Because the training data of permeability was obtained from the direct simulation of fluid flow along the axis direction of the core, we rotated the CT images of the sub-volumes in order to consider the permeability anisotropy. We then applied the trained networks to the rotated sub-volumes to estimate the permeability properties in the perpendicular directions (diagonal elements of the permeability tensor). Note that the off-diagonal elements of permeability tensor are not considered in this study. The estimated permeability (core-axis direction) maps are illustrated in (Fig.11), which indicate that the permeability of sample I is higher than that of sample II. These predicted permeability distributions using the neural network are qualitatively consistent with the ground truth data in Fig.5.

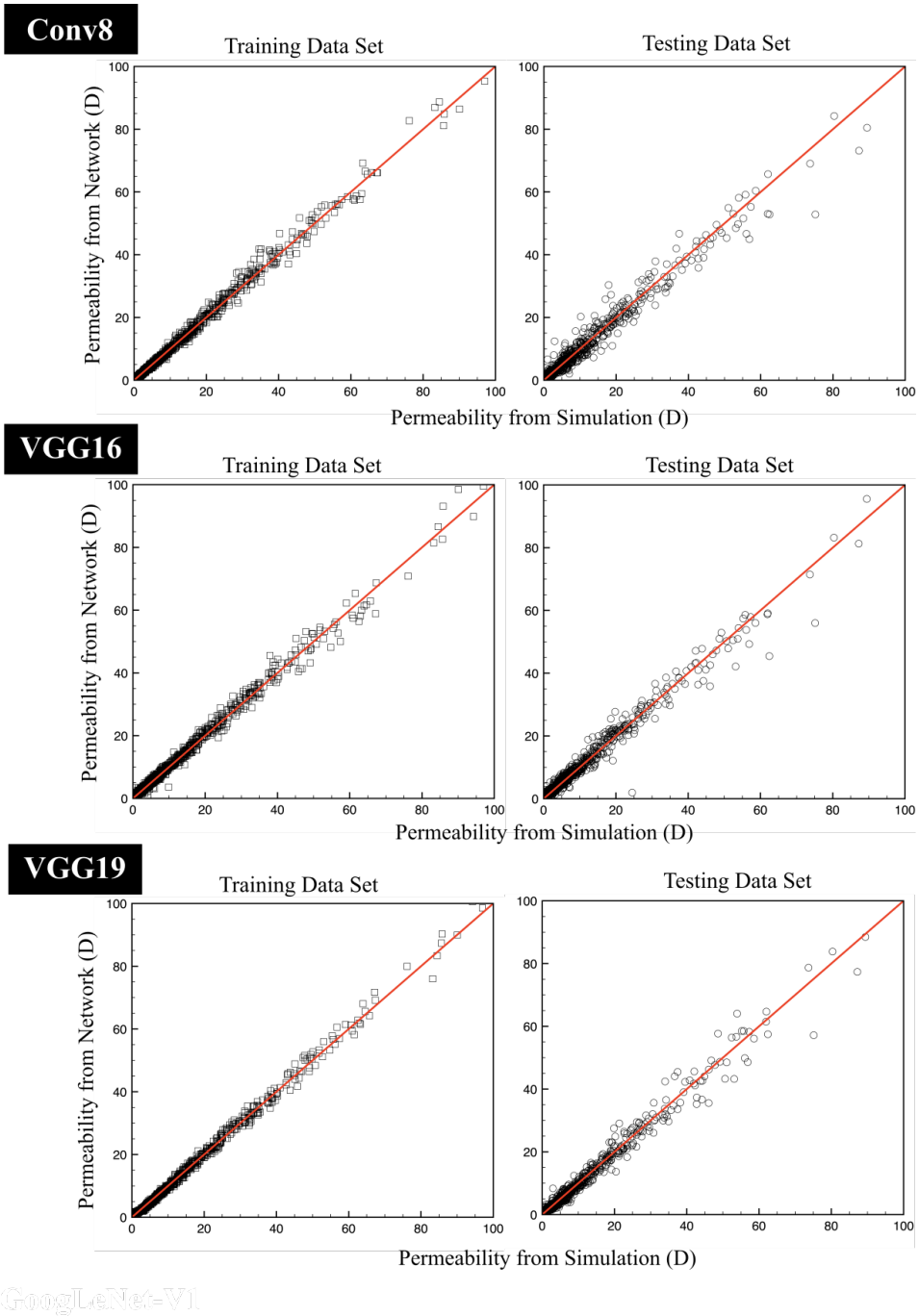

Figure 6. Permeability values from simulation are plotted against the permeability using the network estimation (Conv8, VGG16 and VGG19). The red diagonal line represents $y = x$.

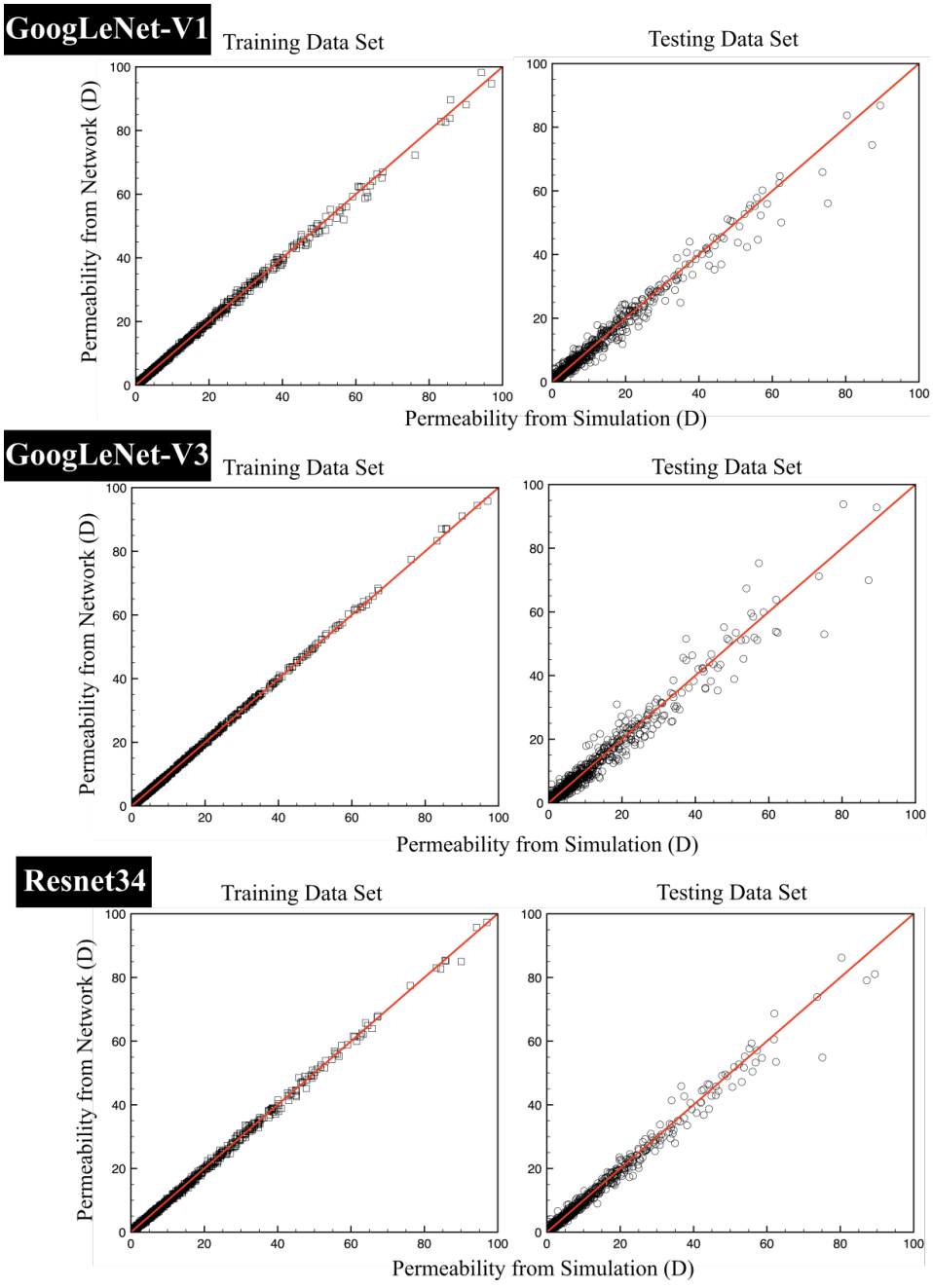

Figure 7. Permeability values from simulation are plotted against the permeability using the network estimation (GoogLeNet-V1, GoogLeNet-V3 and ResNet34). The red diagonal line represents $y = x$.

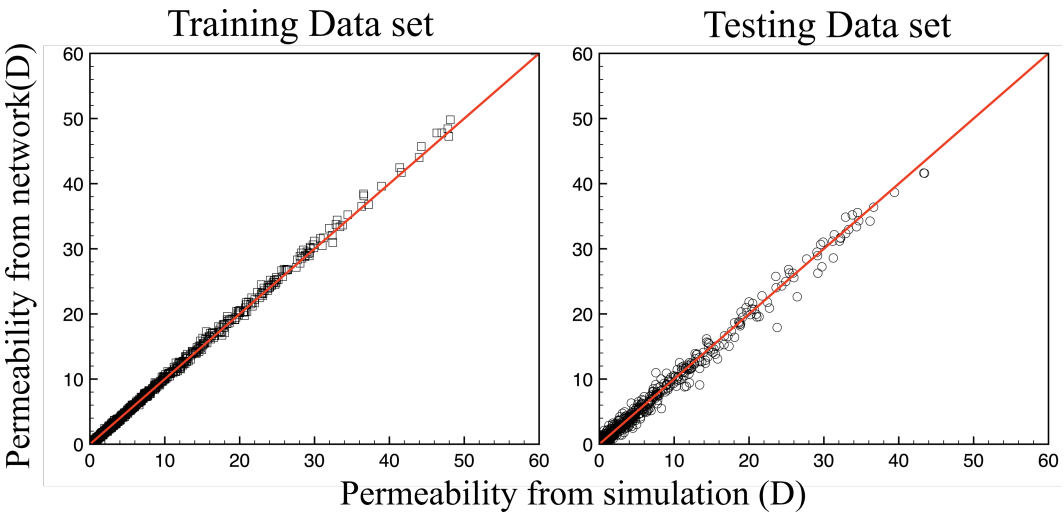

Figure 8. Permeability values from simulation are plotted against the permeability using the Resnet34 network estimation for sample II. The red diagonal line represents $y = x$

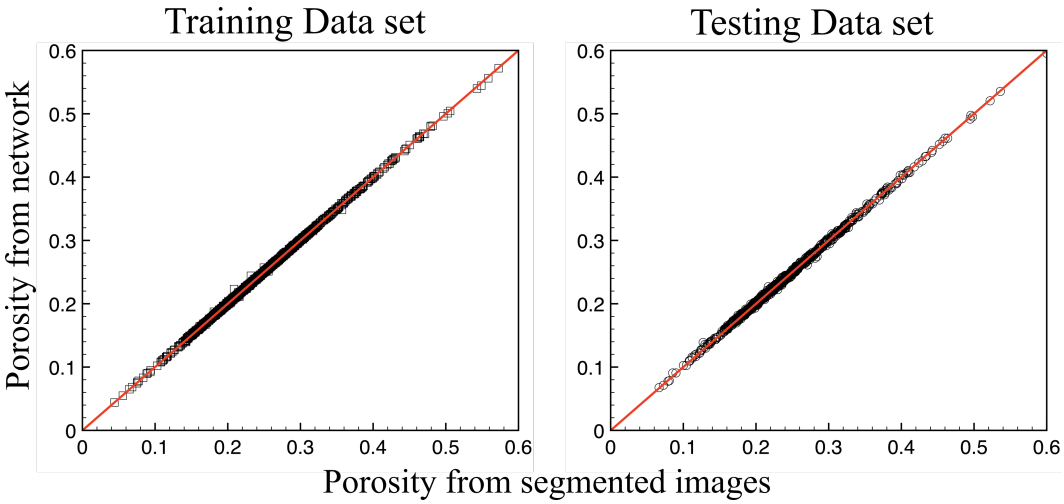

Figure 9. Porosity values from segmented rock images are plotted against the porosity using the Resnet34 network estimation for sample I. The red diagonal line represents $y = x$.

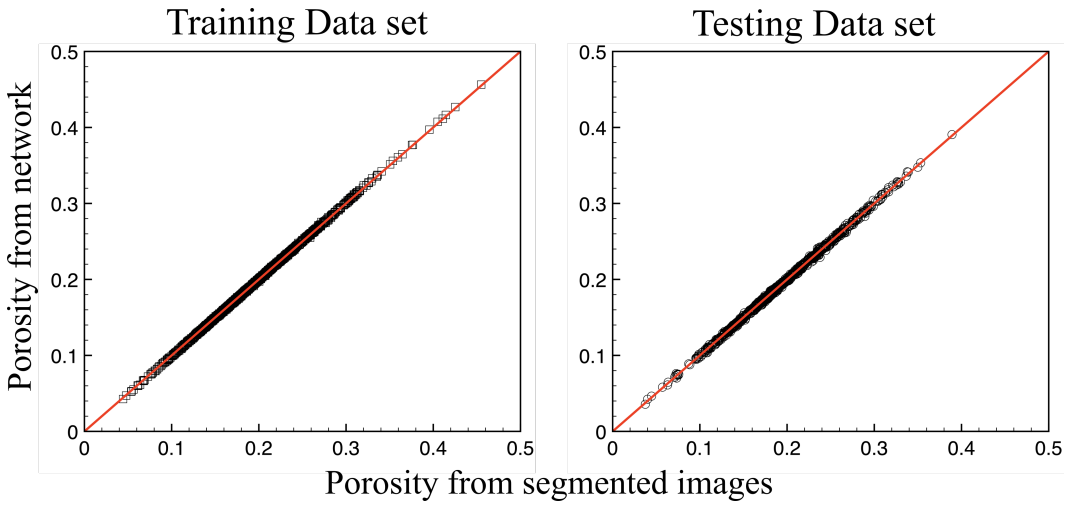

Figure 10. Porosity values from segmented rock images are plotted against the porosity using the Resnet34 network estimation for sample II. The red diagonal line represents $y = x$.

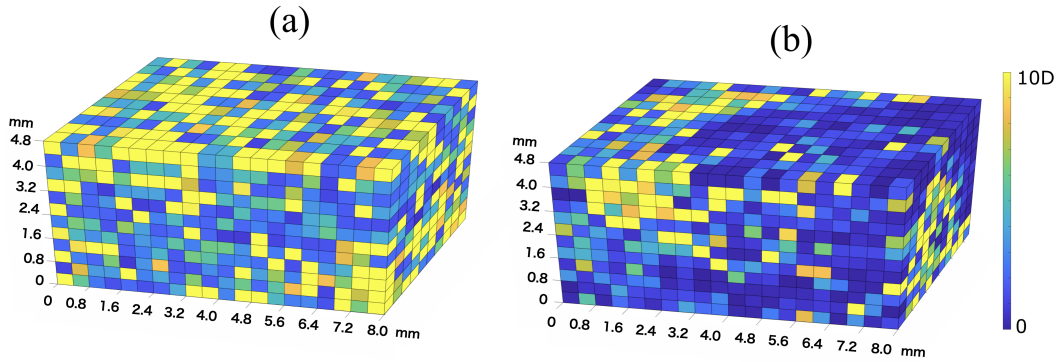

Figure 11. Permeability maps for the whole cores : (a) sample I; (b) sample II.

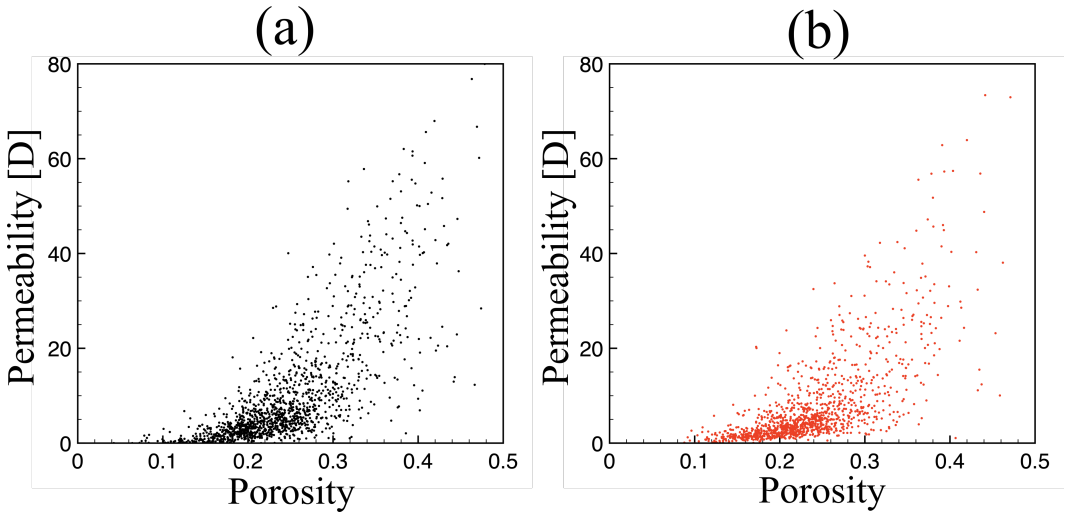

Figure 12. Relationship between the permeability and the porosity for sample I: (a) calculated ground truth data (b) predicted data.

The permeability values mainly depend on porosity. The simplest model describing the permeability-porosity relationship is the Kozeny-Carman (KC) model (CARMAN, 1937). As an evaluation of the capability of our approach, we also checked the permeability-porosity relationship with respect to the predicted results. The plots of predicted porosity-permeability scatters showed a similar pattern with the ground truth data for both samples (Fig.12 and 13). Therefore, our approach can also provide reliable data in terms of the permeability-porosity relationship. Our data-driven approach for predicting permeability and porosity is superior to the empirical KC models, which only related the permeability to porosity neglecting the features of pore microstructures and the effect of flow path connectivity. Besides, the empirical parameter in the KC model is usually not a constant and is difficult to be determined (P. Xu & Yu, 2008). Unlike this conventional empirical model, our CNN-based approach is able to predict the permeability variation considering the effect of microstructures by preserving the information of the original CT images.

This permeability mapping in low-resolution 3D images by using the neural network lays the groundwork for the following permeability upscaling and the computation of effective permeability at the large core scale.

4.6 Upscaled permeability of the whole core

The permeability map is then plugged into the Darcy flow solver (Lie, 2019) to calculate the pressure distribution and flux in the whole sample using the boundary conditions described in Section 3.6. A rectangular cuboid computational domain for the Darcy flow solver is extracted from the core samples with a grids size of $10\times12\times20$. Each grid was assigned the predicted permeabilities in three directions. The gravity was not considered in the Darcy flow simulation. The implementation of this Darcy flow simulation can be found in the reference documentation (*MRST Flow Solver Tutorial*, n.d.). Finally, the solution for flow and pressure in the entire core can be obtained by solving the constructed linear system using two-point flux schemes (Lie, 2019). The results of pressure distribution indicated that the pressure gradient along the flow direction in sample I is relatively uniform (Fig.14) because the permeability map is more homogeneous compared with sample II (Fig. 11). On the contrary, sample II has a relatively heterogeneous per-

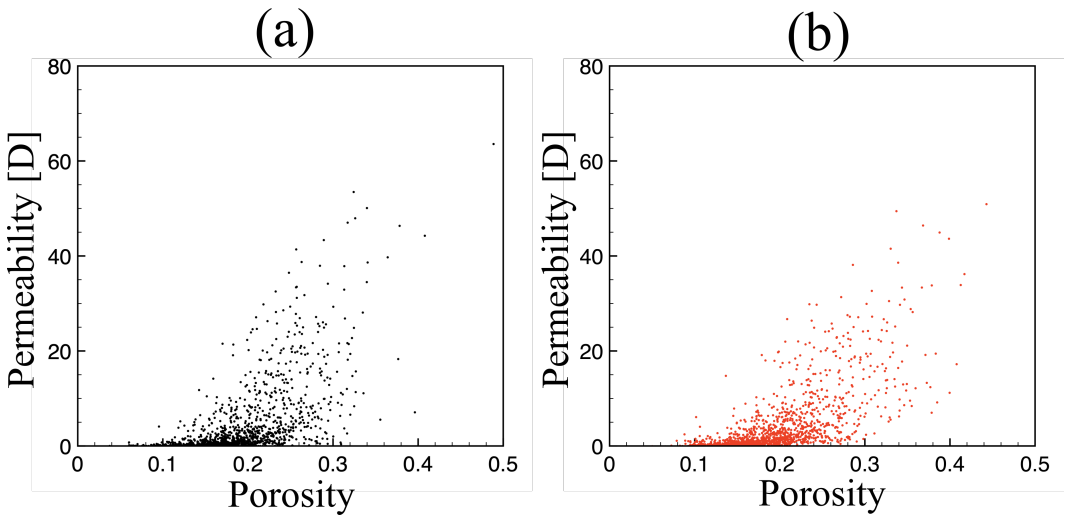

Figure 13. Relationship between the permeability and the porosity for sample II: (a) calculated ground truth data (b) predicted data.

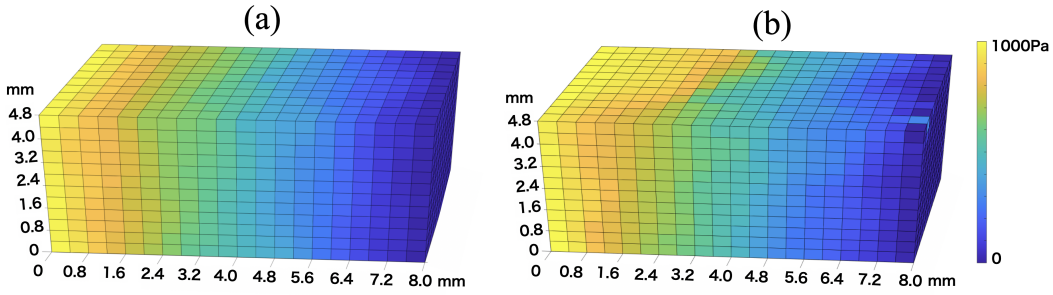

Figure 14. Pressure distributions of the whole core obtained from the Darcy flow solver: (a) sample I (b) sample II.

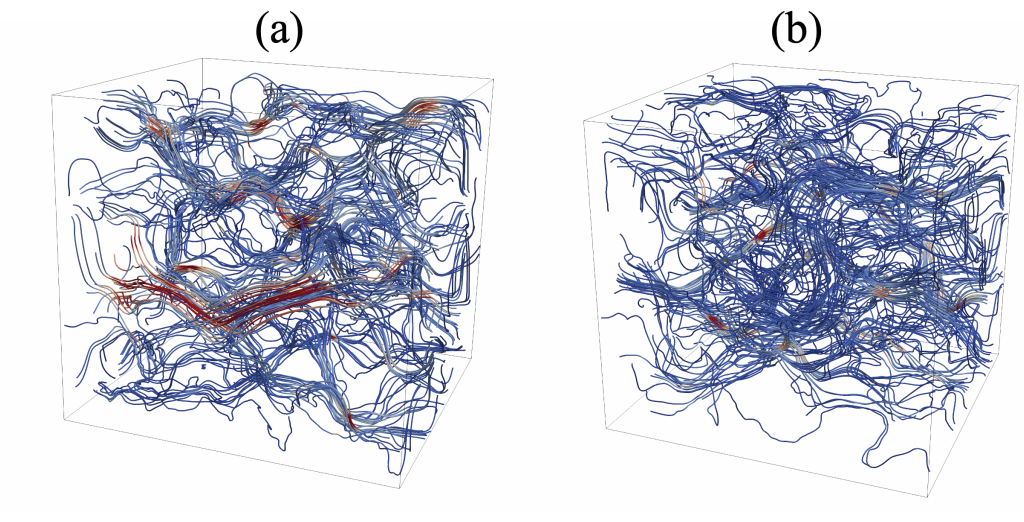

Figure 15. Velocity stream lines of the two center cores obtained from the direct LBM flow simulation: (a) sample I (b) sample II; red and blue colors indicate the high and low velocity cites, respectively .

meability distribution resulting in a non-uniform pressure drop along the flow direction (Fig.14).

Then the upscaled permeability can be calculated from the flux distribution inside the computation domain by the Darcy flow solver. To evaluate the accuracy of the upscaled permeability, we also calculated the permeability at the center region of the same core sample for comparison using the direct LBM flow simulation because only high-resolution micro-CT images of the center area are available. Though, the low-resolution images ($8\mu m$) of the whole core can somehow be segmented for flow simulation to obtain the permeability of the whole area. However, the uncertainty of the segmentation due to the low resolution may lead to a large error in the direct flow simulation. Besides, the domain size of the whole core is too large for LBM simulation, which is beyond the limitation of our computational resources. Therefore, the permeability of only the center core area is fully calculated by LBM simulation as the ground truth reference value. For the Boise sandstone, the simulation domain of $690\times690\times690$ ($1.38mm$ cube) used in the LBM calculation is large enough to reach the REV size. The calculated flow velocity streamlines (Fig. 15) indicated that sample I has highly connected flow paths, which leads to high velocity cites in large pore spaces. On the other hand, the flow velocities in sample II are lower due to the highly tortuous flow paths (Fig. 15). As a result, the permeability of sample II is lower than that of sample I.

We also use pore-network modeling (PNM) to calculate the permeability for the center and the whole core areas with two different resolutions, respectively. PNM is an indirect method that solves simplified transport equations on idealized pore geometries to estimate flow properties (Blunt, 2001). Because the pore geometries in PNM are represented by simple spheres and pipes, the accurate shape of boundaries between pore spaces and solid grain is not necessary. Since the pore structure can still be identified to some extent from the low-resolution images, therefore the PNM can be applied to the whole core area. Here, the pore network rock model is reconstructed by using the skeleton extraction combined with a watershed algorithm (Youssef et al., 2007). The large-scale permeabilities obtained by PNM, LBM, and CNN are summarized in Table. 4.

Sample	I	II
K of center core (PNM; high resolution)	5.15D	0.75D
K of whole core (PNM; low resolution)	12.8D	3.53D
K of center core (LBM; high resolution)	4.83D	1.89D
K of whole core (CNN; low resolution)	5.85D	1.53D

Table 4. Large scale permeabilities K obtained by different methods

The upscaled permeabilities based on CNN agreed well with the data obtained by the LBM, which have relative error of 21% and 19% for samples I and II, respectively. The PNM can roughly estimate the permeability of the center core with high-resolution images but failed to predict the permeability when using low-resolution data. For sample II, the PNM underestimates the permeability even using the high-resolution images. Because sample II has low porosity which means that the size of pore bodies is small, it becomes inaccurate to represent the pore spaces by simple spheres and pipes in PNM. In addition, PNM is highly sensitive to image resolution. In low-resolution images, the pore throats are depicted by intermediate grayscale voxels which may be closed during the segmentation process. Such uncertainties in the segmentation process for low-resolution images leads to large errors in PNM predictions. On the other hand, our upscaling method direct utilized the raw low-resolution images without the segmentation process, and therefore preserves the grayscale information related to pore, results in higher accuracy in predicting the permeability. The measured permeability of the Boise sandstone by the experiment performed on a meter scale is 2.8D, which is between the predicted values of the two samples. This is reasonable because samples I and II are extracted from the high and low porosity areas, respectively. Therefore, we can conclude that our CNN-based upscaling method is able to estimate the reliable value of permeability at a large scale.

Since both samples I and II are extracted from the same Boise sandstone core at different locations, the general features of the pore structures of these two samples may have similarities. Therefore, we also tested the prediction performance for the permeability map of sample II using the neural network trained by the data extracted from sample I (i.e., using the best network weights obtained from the training process of sample I). The predicted permeability map of sample II (Fig.16) presented a very similar distribution to the native permeability map (Fig.11(b)), namely, the predicted permeability map using the CT images and the neural network trained by the data from the same sample. The upscaled permeability of sample II from the permeability map predicted by the sample I's network is 2.47D, which is slightly overestimated compared with the ground-truth value (1.53D) because most of the training data in sample I has higher porosity and permeability than sample II. Nevertheless, the accuracy is still much better than that obtained by PNM. The upscaled permeability predicted by the combination of sample II's geometry (CT images) and sample I's neural network is very close to the experimental data (2.8D).

From the above investigation, we can conclude that the trained neural network is applicable for the unseen sample of the same rock type (Boise sandstone used here). However, it must be mentioned that, for the other rock types, we need to carry out the same deep learning process again to establish a specialized well-trained neural network because different rock types usually have different characteristics of pore geometry (e.g., pore connectivities and porosities) which leads to different weights of the neuron. Finally, we could build a trained neuron network database for each type of rock, which enables us to quickly estimate the permeability directly from the raw CT images without carrying out the costly and time-consuming experiment.

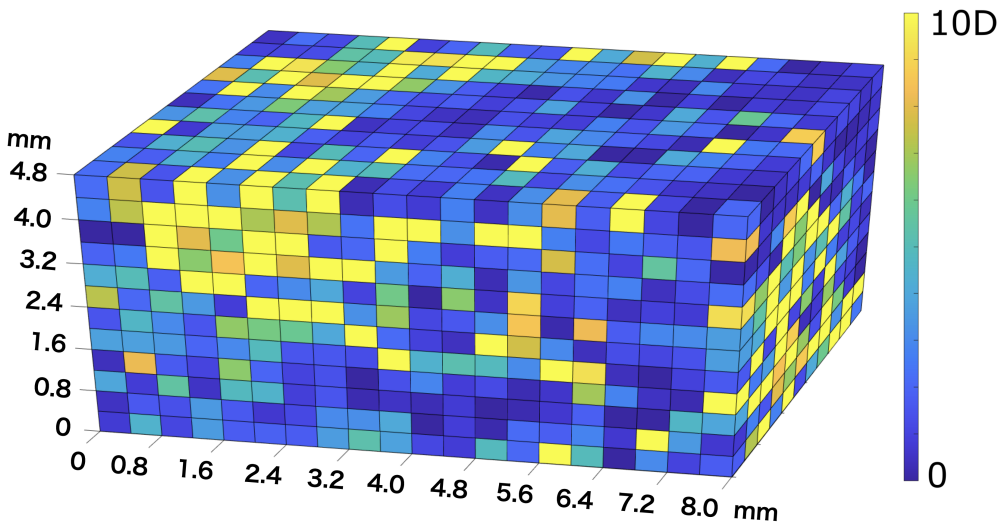

Figure 16. Permeability map of the sample II predicted by the neural network trained using data extracted from sample I.

5 Summary

This study presented a workflow to predict the upscaled absolute permeability of the large rock core directly from CT images whose resolution is insufficient to allow direct permeability computation. Our approach used a deep learning technique to establish correlations between low-resolution image characteristics and high-resolution computed permeability by overlapping registered CT images. The training data sets for deep learning consist of pairs of coarse scanned raw CT images and their corresponding permeability value obtained by performing LBM simulation on high-resolution CT images. During this process, image registration is vital for integrating micro-CT images acquired at two different resolutions. Six different neural networks were trained to check the performance for predicting the permeability of the low-resolution images. The Resnet showed the best performance and can accurately predict the spatial variations of both porosity and permeability properties. The permeability map of large field of view can be directly obtained from the raw low-resolution CT images by the neural networks without the segmentation process. Based on the permeability map, the upscaled permeability of the entire core can be calculated by the Darcy flow solver. The upscaled permeability showed a good agreement with the experiment data, which indicates that our deep-learning-based upscaling method allows estimating the large-scale permeability of core samples while preserving the effects of fine-scale variations due to local heterogeneity.

6 Acknowledgement

We gratefully acknowledge funding from Japan Oil, Gas and Metals National Corporation (JOGMEC). This study was also supported by the Japan Society for the Promotion of Science (JSPS) through a Grant-in-Aid for Challenging Exploratory Research (Grant No. JP20K20948) and a Grant-in-Aid for Scientific Research (Grant No. JP22K03927).

7 Data Availability Statement

The datasets and code used in this study are available from Mendeley repository `http://dx.doi.org/10.17632/7jmfszpws7.1`

Appendix A Neural network architectures

The architectures of neural network using in this study are presented here. In the following figures, relu refers to the rectified linear unit activation (Nair & Hinton, 2010). The blocks with five numbers inside indicate the convolution layer, in which the first three numbers refer to the kernel size in three dimensions, the second number means stride size, and the last shows the filter number. MP means the max pooling layer with kernel size shown in the block. BN refers to batch normalization (Ioffe & Szegedy, 2015), GP means the global average pooling layer, FC means filter concatenation, and DP in the dense block refers to the dropout layer applied after the dense layer. The dense layer size is shown at the top of the dense block.

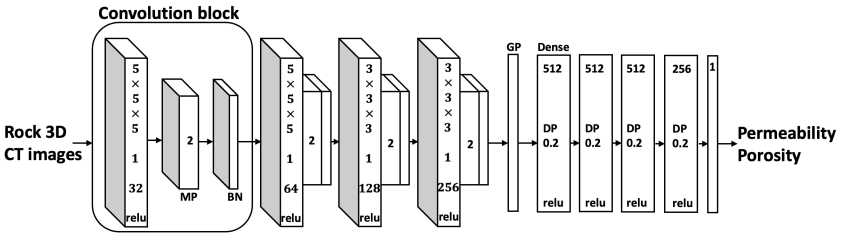

Figure A1. Conv8 network architecture.

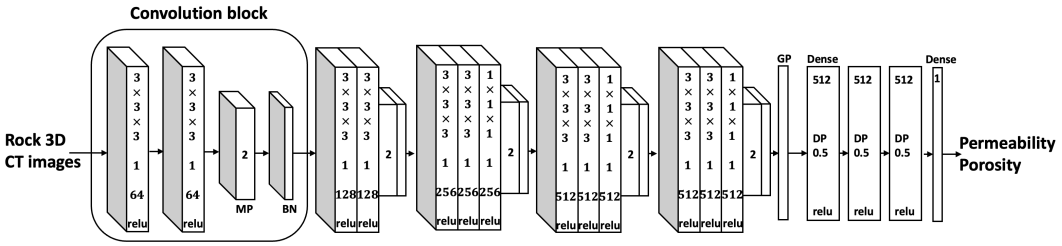

Figure A2. VGG16 network architecture

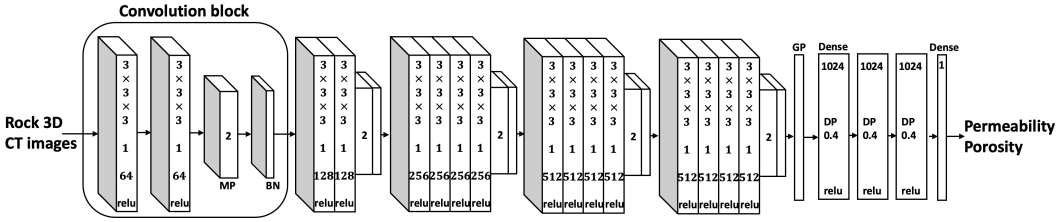

Figure A3. VGG19 network architecture

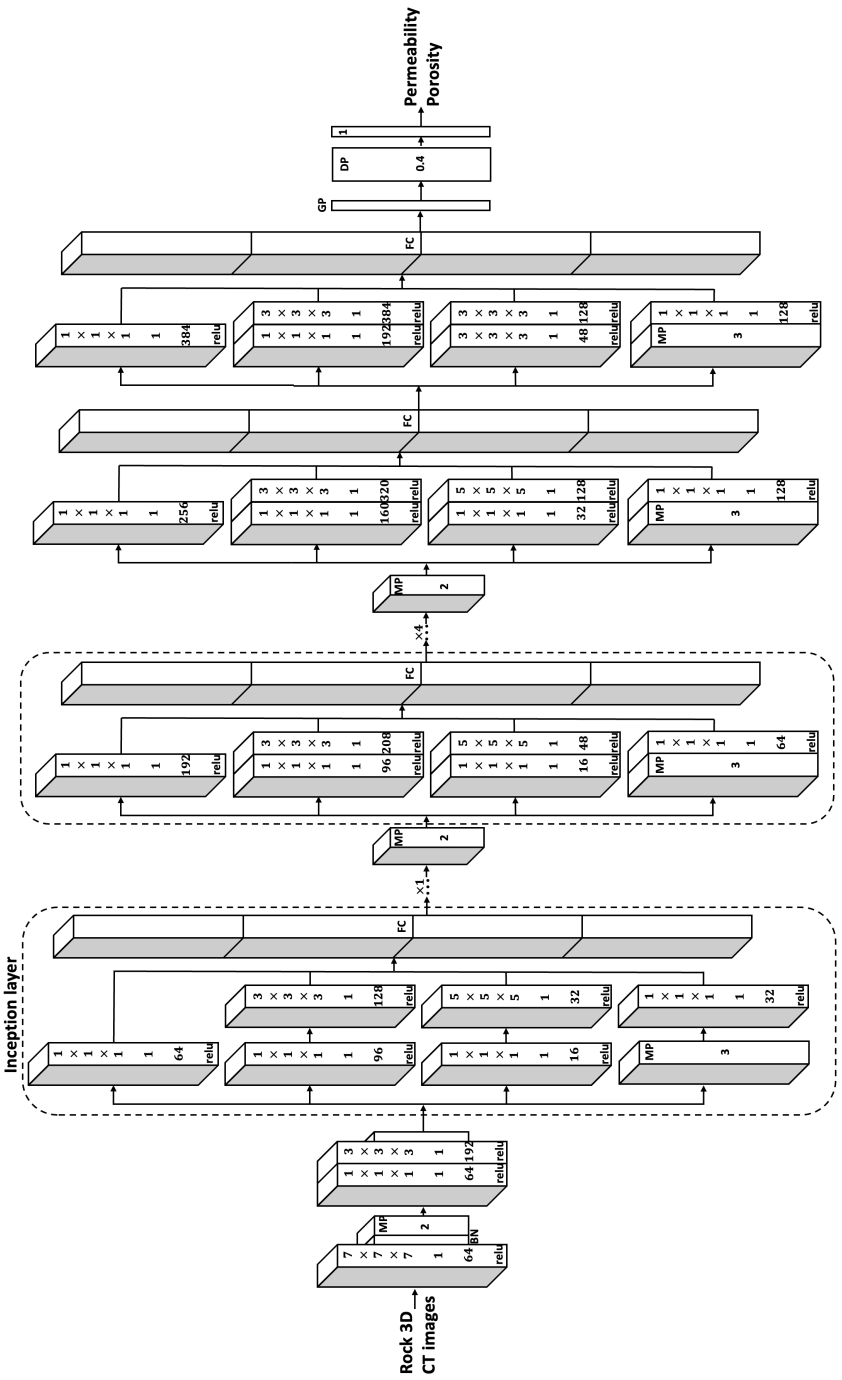

Figure A4. GoogLeNet-V1 network architecture

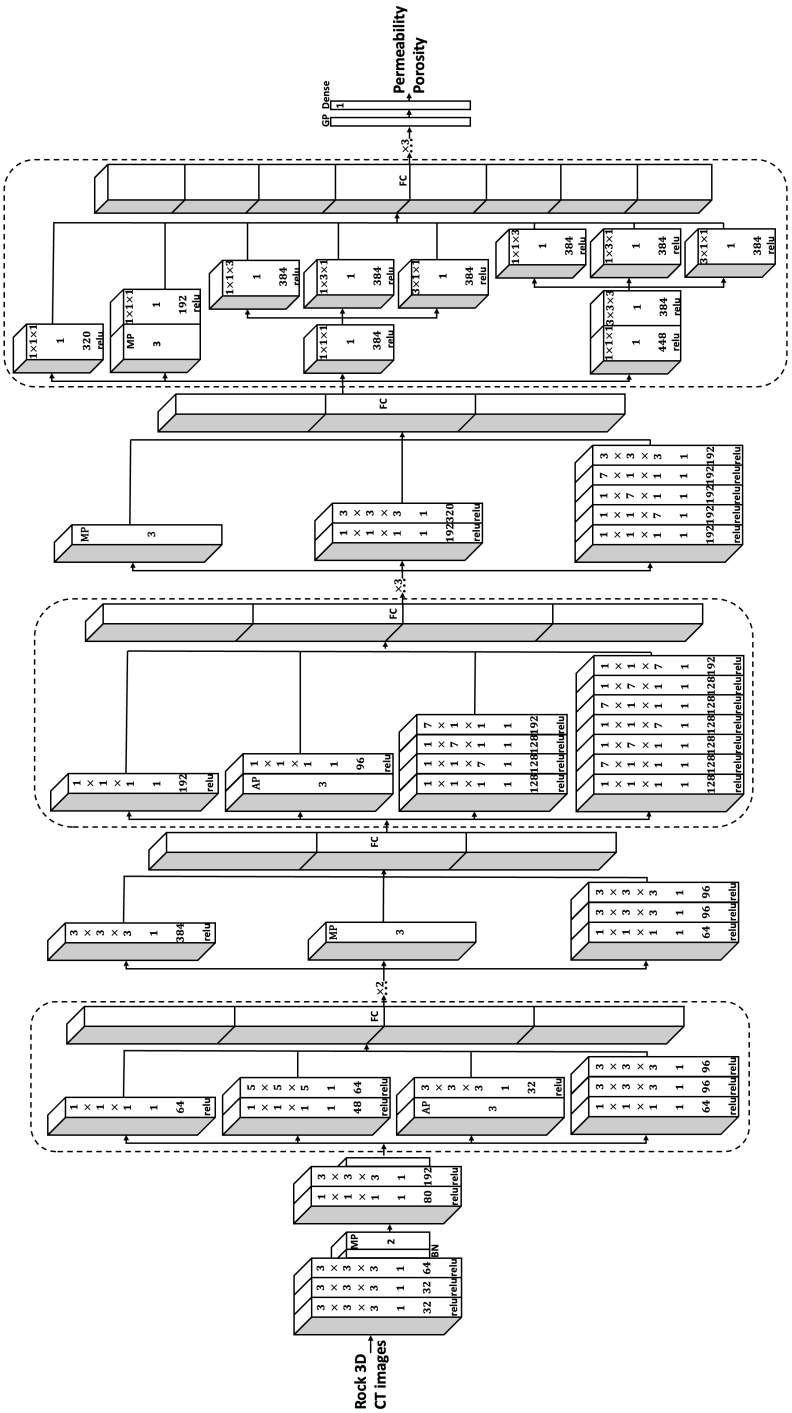

Figure A5. GoogLeNet-V3 network architecture

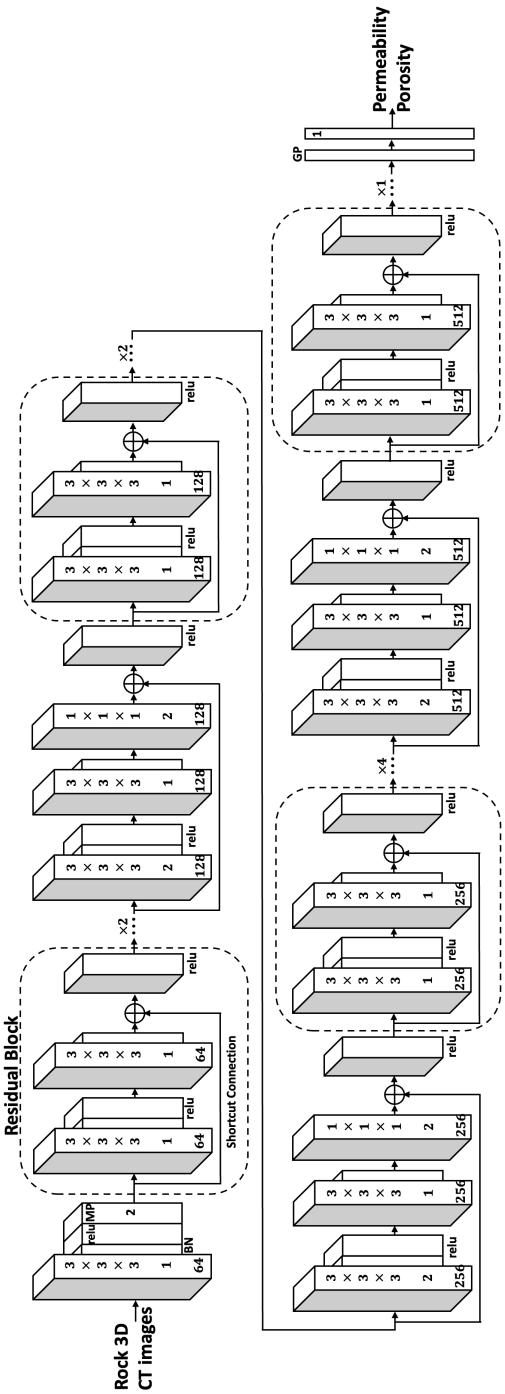

Figure A6. Resnet34 network architecture

References

Abadi, M., Agarwal, A., Barham, P., Brevdo, E., Chen, Z., Citro, C., ... Zheng, X. (2015). *TensorFlow: Large-scale machine learning on heterogeneous systems.* Retrieved from `http://tensorflow.org/` (Software available from tensorflow.org)

Alqahtani, N., Alzubaidi, F., Armstrong, R. T., Swietojanski, P., & Mostaghimi, P.

(2020). Machine learning for predicting properties of porous media from 2d x-ray images. *Journal of Petroleum Science and Engineering*, *184*, 106514.

Alqahtani, N. J., Chung, T., Wang, Y. D., Armstrong, R. T., Swietojanski, P., & Mostaghimi, P. (2021). Flow-based characterization of digital rock images using deep learning. *SPE Journal*, *26*(04), 1800–1811.

Arns, C. H., Knackstedt, M. A., Pinczewski, M. V., & Lindquist, W. (2001). Accurate estimation of transport properties from microtomographic images. *Geophysical research letters*, *28*(17), 3361–3364.

Bizhani, M., Ardakani, O. H., & Little, E. (2022). Reconstructing high fidelity digital rock images using deep convolutional neural networks. *Scientific reports*, *12*(1), 1–14.

Blunt, M. J. (2001). Flow in porous media—pore-network models and multiphase flow. *Current opinion in colloid & interface science*, *6*(3), 197–207.

Blunt, M. J., Bijeljic, B., Dong, H., Gharbi, O., Iglauer, S., Mostaghimi, P., ... Pentland, C. (2013). Pore-scale imaging and modelling. *Advances in Water resources*, *51*, 197–216.

Boek, E. S., & Venturoli, M. (2010). Lattice-boltzmann studies of fluid flow in porous media with realistic rock geometries. *Computers & Mathematics with Applications*, *59*(7), 2305–2314.

Botchkarev, A. (2018). Performance metrics (error measures) in machine learning regression, forecasting and prognostics: Properties and typology. *arXiv preprint arXiv:1809.03006*.

Botha, P. W., & Sheppard, A. P. (2016). Mapping permeability in low-resolution micro-ct images: A multiscale statistical approach. *Water Resources Research*, *52*(6), 4377–4398.

CARMAN, P. C. (1937). Fluid flow through granular beds. *Trans. Inst. Chem. Eng.*, *15*, 150-166. Retrieved from `https://ci.nii.ac.jp/naid/10003392892/`

Da Wang, Y., Armstrong, R. T., & Mostaghimi, P. (2019). Enhancing resolution of digital rock images with super resolution convolutional neural networks. *Journal of Petroleum Science and Engineering*, *182*, 106261.

Dehghan Khalili, A., Arns, J.-Y., Hussain, F., Cinar, Y., Pinczewski, W., Arns, C. H., et al. (2013). Permeability upscaling for carbonates from the pore scale by use of multiscale x-ray-ct images. *SPE Reservoir Evaluation & Engineering*, *16*(04), 353–368.

d'Humières, D. (1992). Generalized lattice-boltzmann equations. *Rarefied gas dynamics*.

Fredrich, J., Greaves, K., & Martin, J. (1993). Pore geometry and transport properties of fontainebleau sandstone. In *International journal of rock mechanics and mining sciences & geomechanics abstracts* (Vol. 30, pp. 691–697).

Goral, J., Walton, I., Andrew, M., & Deo, M. (2019). Pore system characterization of organic-rich shales using nanoscale-resolution 3d imaging. *Fuel*, *258*, 116049.

Guo, Z., & Shu, C. (2013). *Lattice boltzmann method and its application in engineering* (Vol. 3). World Scientific.

He, K., Zhang, X., Ren, S., & Sun, J. (2016). Deep residual learning for image recognition. In *Proceedings of the ieee conference on computer vision and pattern recognition* (pp. 770–778).

Hong, J., & Liu, J. (2020, August). Rapid estimation of permeability from digital rock using 3D convolutional neural network. *Computational Geosciences*, *24*(4), 1523–1539. doi: 10.1007/s10596-020-09941-w

Huber, P. J. (1992). Robust estimation of a location parameter. In *Breakthroughs in statistics* (pp. 492–518). Springer.

Ioffe, S., & Szegedy, C. (2015). Batch normalization: Accelerating deep network training by reducing internal covariate shift. In *International conference on*

machine learning (pp. 448–456).

Jiang, F., Liu, H., Chen, X., & Tsuji, T. (2022). A coupled lbm-dem method for simulating the multiphase fluid-solid interaction problem. *Journal of Computational Physics*, 110963.

Jiang, F., Matsumura, K., Ohgi, J., & Chen, X. (2021). A gpu-accelerated fluid–structure-interaction solver developed by coupling finite element and lattice boltzmann methods. *Computer Physics Communications*, *259*, 107661.

Jiang, F., & Tsuji, T. (2014). Changes in pore geometry and relative permeability caused by carbonate precipitation in porous media. *Physical Review E*, *90*(5), 053306.

Jiang, F., & Tsuji, T. (2015). Impact of interfacial tension on residual co2 clusters in porous sandstone. *Water Resources Research*, *51*(3), 1710–1722.

Jiang, F., & Tsuji, T. (2017). Estimation of three-phase relative permeability by simulating fluid dynamics directly on rock-microstructure images. *Water Resources Research*, *53*(1), 11–32.

Juanes, R., Spiteri, E., Orr Jr, F., & Blunt, M. (2006). Impact of relative permeability hysteresis on geological co2 storage. *Water resources research*, *42*(12).

Lake, L. W., Johns, R., Rossen, B., Pope, G. A., et al. (2014). *Fundamentals of enhanced oil recovery* (Vol. 1). Society of Petroleum Engineers Richardson, TX.

LeCun, Y., Bottou, L., Bengio, Y., & Haffner, P. (1998). Gradient-based learning applied to document recognition. *Proceedings of the IEEE*, *86*(11), 2278–2324.

Li, S., Jiang, F., Wei, B., Hou, J., & Liu, H. (2021). Prediction of three-phase relative permeabilities of berea sandstone using lattice boltzmann method. *Physics of Fluids*, *33*(6), 063302.

Lie, K.-A. (2019). Single-phase flow. In *An introduction to reservoir simulation using matlab/gnu octave: User guide for the matlab reservoir simulation toolbox (mrst)* (p. 111–112). Cambridge University Press.

Liu, H., Lu, Y., Li, S., Yu, Y., & Sahu, K. C. (2021). Deformation and breakup of a compound droplet in three-dimensional oscillatory shear flow. *International Journal of Multiphase Flow*, *134*, 103472.

Menke, H. P., Maes, J., & Geiger, S. (2021, December). Upscaling the porosity–permeability relationship of a microporous carbonate for Darcy-scale flow with machine learning. *Scientific Reports*, *11*(1), 2625. doi: 10.1038/s41598-021-82029-2

MRST Flow Solver Tutorial. (n.d.). `https://www.sintef.no/projectweb/mrst/documentation/tutorials/flow-solver-tutorial/`.

Nair, V., & Hinton, G. E. (2010). Rectified linear units improve restricted boltzmann machines. In *Icml.*

Pan, C., Luo, L.-S., & Miller, C. T. (2006). An evaluation of lattice boltzmann schemes for porous medium flow simulation. *Computers & fluids*, *35*(8-9), 898–909.

Pape, H., Clauser, C., & Iffland, J. (1999). Permeability prediction based on fractal pore-space geometry. *Geophysics*, *64*(5), 1447–1460.

Rabbani, A., & Babaei, M. (2019). Hybrid pore-network and lattice-boltzmann permeability modelling accelerated by machine learning. *Advances in water resources*, *126*, 116–128.

Raeini, A. Q., Blunt, M. J., & Bijeljic, B. (2012). Modelling two-phase flow in porous media at the pore scale using the volume-of-fluid method. *Journal of Computational Physics*, *231*(17), 5653–5668.

Rumelhart, D. E., Hinton, G. E., & Williams, R. J. (1986). Learning representations by back-propagating errors. *nature*, *323*(6088), 533–536.

Santos, J. E., Xu, D., Jo, H., Landry, C. J., Prodanović, M., & Pyrcz, M. J. (2020, April). PoreFlow-Net: A 3D convolutional neural network to predict fluid flow through porous media. *Advances in Water Resources*, *138*, 103539. doi: 10.1016/j.advwatres.2020.103539

Shah, S., Gray, F., Crawshaw, J., & Boek, E. (2016). Micro-computed tomography pore-scale study of flow in porous media: Effect of voxel resolution. *Advances in water resources*, *95*, 276–287.

Shan, X., Yuan, X.-F., & Chen, H. (2006). Kinetic theory representation of hydrodynamics: a way beyond the navier–stokes equation. *Journal of Fluid Mechanics*, *550*, 413–441.

Simonyan, K., & Zisserman, A. (2014). Very deep convolutional networks for large-scale image recognition. *arXiv preprint arXiv:1409.1556*.

Suzuki, A., Fukui, K.-i., Onodera, S., Ishizaki, J., & Hashida, T. (2022). Data-driven geothermal reservoir modeling: Estimating permeability distributions by machine learning. *Geosciences*, *12*(3), 130.

Szegedy, C., Liu, W., Jia, Y., Sermanet, P., Reed, S., Anguelov, D., ... Rabinovich, A. (2015). Going deeper with convolutions. In *Proceedings of the ieee conference on computer vision and pattern recognition* (pp. 1–9).

Tester, J. W., Anderson, B. J., Batchelor, A., Blackwell, D., DiPippo, R., Drake, E., ... others (2006). The future of geothermal energy. *Massachusetts Institute of Technology*, *358*.

Wang, Y. D., Blunt, M. J., Armstrong, R. T., & Mostaghimi, P. (2021, April). Deep learning in pore scale imaging and modeling. *Earth-Science Reviews*, *215*, 103555. doi: 10.1016/j.earscirev.2021.103555

Wang, Y. D., Shabaninejad, M., Armstrong, R. T., & Mostaghimi, P. (2021). Deep neural networks for improving physical accuracy of 2d and 3d multi-mineral segmentation of rock micro-ct images. *Applied Soft Computing*, *104*, 107185. Retrieved from `https://www.sciencedirect.com/science/article/pii/S1568494621001083` doi: https://doi.org/10.1016/j.asoc.2021.107185

Worthington, P. F. (2004). The effect of scale on the petrophysical estimation of intergranular permeability. *Petrophysics-The SPWLA Journal of Formation Evaluation and Reservoir Description*, *45*(01), 59–72.

Xu, P., & Yu, B. (2008). Developing a new form of permeability and kozeny–carman constant for homogeneous porous media by means of fractal geometry. *Advances in water resources*, *31*(1), 74–81.

Xu, Z.-J. (2012). Homogenization and upscaling for diffusion, heat conduction, and wave propagation in heterogeneous materials. *Communications in Theoretical Physics*, *57*(3), 348.

Yang, J., & Boek, E. S. (2013). A comparison study of multi-component lattice boltzmann models for flow in porous media applications. *Computers & Mathematics with Applications*, *65*(6), 882–890.

Yang, L., Yang, J., Boek, E., Sakai, M., & Pain, C. (2019). Image-based simulations of absolute permeability with massively parallel pseudo-compressible stabilised finite element solver. *Computational Geosciences*, *23*(5), 881–893.

You, N., Li, Y. E., & Cheng, A. (2021). 3d carbonate digital rock reconstruction using progressive growing gan. *Journal of Geophysical Research: Solid Earth*, *126*(5), e2021JB021687.

Youssef, S., Rosenberg, E., Gland, N. F., Kenter, J. A., Skalinski, M., & Vizika, O. (2007). High resolution ct and pore-network models to assess petrophysical properties of homogeneous and heterogeneous carbonates. In *Spe/eage reservoir characterization and simulation conference.*

Zhai, H., Xue, Z., Park, H., Aizawa, Y., Baba, Y., & Zhang, Y. (2020). Migration characteristics of supercritical co2 microbubble flow in the berea sandstone revealed by voxel-based x-ray computed tomography imaging analysis. *Journal of Natural Gas Science and Engineering*, *77*, 103233.

Zhang, Y., Jiang, F., & Tsuji, T. (2022). Influence of pore space heterogeneity on mineral dissolution and permeability evolution investigated using lattice boltzmann method. *Chemical Engineering Science*, *247*, 117048.